Antiferromagnetism of the cation-ordered warwickite system $Mn_{2-x}Mg_xBO_4$ (x = 0.55, 0.63 or 0.67)

N.V. Kazak[1*], N.A. Belskaya[2], E.M. Moshkina[1], L.N. Bezmaternykh[1], A.D. Vasiliev[1], S.N. Sofronova[1], R.M. Eremina[3,4], E.V. Eremin[1], A.R. Muftakhutdinov [4], M.A. Cherosov[4] and S.G. Ovchinnikov[1]

[1]Kirensky Institute of Physics, FRC SB RAS, Krasnoyarsk, Russia

[2]Reshetnev Siberian State University of Science and Technology, Krasnoyarsk, Russia

[3]Zavoisky Physical-Technical Institute, FRC Kazan Scientific Centre of RAS, Kazan, Russia

[4]Kazan (Volga Region) Federal University, Kazan, Russia

Corresponding author:

Dr. Natalia Kazak

Laboratory of Physics of Magnetic Phenomena

Kirensky Institute of Physics, Federal Research Center KSC SB RAS

Academgorodok 50/38, Krasnoyarsk, 660036, Russia

+7(391)249-45-56

nat@iph.krasn.ru

Highlights

- Single crystals of $Mn_{2-x}Mg_xBO_4$ (x=0.55, 0.63, and 0.67) solid solutions were obtained using flux synthesis.
- A monoclinic P121/n1 symmetry similar to the end member Mn_2BO_4 is found for all samples.
- Regular cation and charge distributions over two non-equivalent metal sites are observed.
- DC magnetization and heat capacity measurements reveal an AFM ordering at T_N= 16, 14 and 13 K for x=0.55, 0.63, and 0.67, respectively.
- The prerequisites for the occurrence of cation and magnetic orderings in heterometallic warwickites are discussed.

Abstract: X-ray diffraction, heat capacity and magnetic measurements are performed on single crystals of $Mn_{2-x}Mg_xBO_4$ (x = 0.55, 0.63 or 0.67) with the warwickite structure. The monoclinic symmetry is found for all samples with the space group P121/n1. The M1 site is occupied by trivalent Mn ions while the M2 site is occupied by a mixture of divalent Mg and Mn ions. Regular cation and charge distributions are observed, which is unusual for heterometallic warwickites. The local octahedral distortions of $M1O_6$ show the monotonic dependence on the Mg content and are in accordance with the Jahn-Teller distortion. All samples are found to undergo long-range antiferromagnetic ordering with rather low transition temperatures of T_N = 16, 14 and 13 K for x=0.55, 0.63, and 0.67, respectively. The ordering of local octahedral distortions, caused by the strong electron-phonon interaction of the trivalent Mn ions, is proposed to stabilise the cationic ordering and, as a result, the long-range magnetic ordering in the material.

Keywords: warwickites, antiferromagnet, cation ordering, Jahn-Teller distortions

1. Introduction

Transition-metal oxyborates represent a common mineral class. These minerals are formed at all stages of geological processes, which is the reason for the significant interest in these systems from geophysical and geochemical points of view. For example, the isomorphic pair of $2Fe^{3+}$-$(Mg^{2+}+Ti^{4+})$ forms a continuous row of solid solutions of rock-forming minerals: Mg_2FeBO_5 ludwigite – Fe_3BO_5 vonsenite [1], $Mg_{1.5}Ti_{0.5}BO_4$ warwickite – $MgFeBO_4$ yuanfuliite [2]. Moreover, these materials are also of interest with regards to fundamental physics. The strong relationship between the spin, orbital and lattice degrees of freedom allows for observations of a variety of cooperative phenomena, including charge and orbital ordering, cascades of magnetic phase transitions, structural transformations accompanied by conductivity anomalies and charge density waves formation [3–10]. A number of recent studies have demonstrated the potential of borates as high capacity cathode materials for Li and Na batteries [11-13].

Recently, a significant attention has been devoted to complex oxyborates that are isostructural to ludwigite and warwickite minerals [14–16]. The general formula of these compounds is $M^{2+}{}_nM^{3+}O_nBO_3$, where n = 1 for the warwickites and n = 2 for the ludwigites. Metallic ions occupy $2{\cdot}n$ crystallographic non-equivalent positions and have octahedral oxygen coordination (Fig. 1). A notable peculiarity of these materials is the tendency of the di- and trivalent ions to form ordered planes parallel to the short crystallographic direction (a crystal parameter of c = ~3 Å). The ratio of di- and trivalent ions per formula unit determines the ability of the system to form the ordered planes. Therefore, in the ludwigites, where $M^{2+}/(B^{3+}, M^{3+})$ =

1:1, the divalent ions filling the 1, 2 and 3 metal sites build the planes spatially separated by the planes of trivalent ions (boron and M^{3+} ions at site 4). Warwickites, where this ratio is 1:2, are prone to forming mixed cation planes.

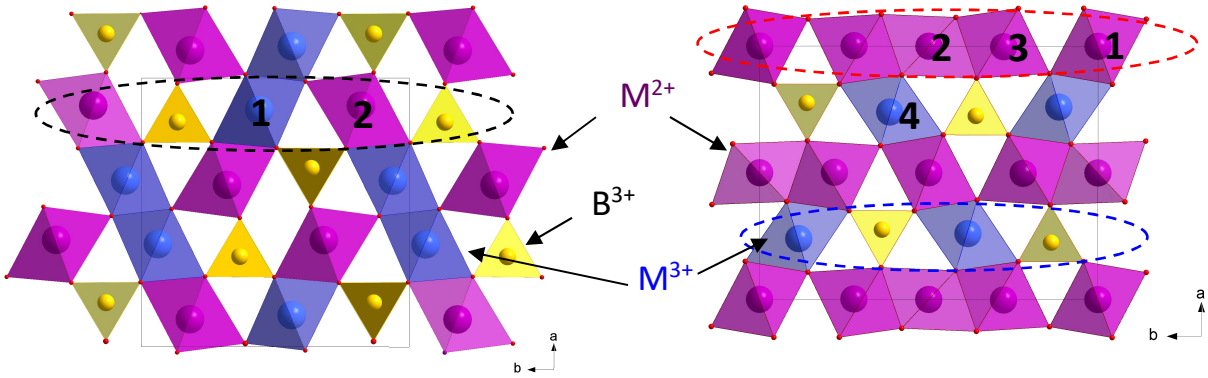

Fig. 1. Crystal structures of M_2BO_4 (left, Pnam(No.62)) and M_3BO_5 (right, Pbam(No.55)) with warwickite and ludwigite structures, respectively. The edge-sharing octahedra occupied by M^{2+} and M^{3+} ions are highlighted by pink and blue, respectively. The distinct crystallographic sites are numbered. The B^{3+} ions are at the centre of the trigonal BO_3 groups (yellow triangles). Dashed lines show the different types of cation planes: space-separated planes of di- and trivalent ions in the ludwigite structure and valence-mixed planes in the warwickite structure.

The distribution of the di- and trivalent cations over distinct metal sites determines the oxidation states at a particular site and, ultimately, the magnetic ground state. Thus, the ludwigites tend to exhibit long-range order. For example, $M^{2+}{}_2Fe^{3+}BO_5$ (M^{2+} = Fe or Co) shows cascade magnetic transitions associated with the magnetic ordering of two spin ladders (3-1-3 and 4-2-4) at Neel temperatures T_{N1} = 112 K (PM-AFM) and T_{N2} = 74 K (AFM-Ferri), respectively [4,5]. In Co_3BO_5, the Co^{3+} ions exclusively filling the M4 site are in the low-spin state (d^6, S = 0) that makes this oxyborate a ferrimagnet with T_N = 42 K [5,6].

Unlike ludwigites, warwickites show a much stronger tendency for cationic disorder and are classified at intrinsically disordered systems. The numerous heterometallic warwickites are magnetically disordered systems. They undergo the transition to the spin-glass state with the intermediate temperature phase – random exchange Heisenberg antiferromagnetic chains [8,9,17,18] or demonstrate the properties of the random singlet phase [19]. The effects of the magnetic frustrations arising from the cation disorder and the crystal structure peculiarities are manifested in the extremely high parameter of magnetic frustration $\eta = \frac{\theta}{T_{SG}} > 10$ [9,17]. In contrast, homometallic warwickites demonstrate a long-range order. So far, only three of six hypothetically possible homometallic warwickites (M^{2+} = M^{3+} = Ti, V, Cr, Mn, Fe or Co) have been synthesised, namely, Mn_2BO_4 [20, 21], Fe_2BO_4 [22] and V_2BO_4 [23]. All of them demonstrate cationic and charge orderings. The transition to the charge ordering phase is

accompanied by the orthorhombic → monoclinic symmetry lowering. This suggests that the long-range magnetic order in the warwickites is determined by the cation order and as a consequence by the charge state at the particular metal site. If so, then the following questions arise: i) is it possible to achieve long-range magnetic order in the heterometallic warwickites?; ii) how can the cation order in these systems be reached?

As an initial focus, the Mn_2BO_4 homometallic system has been chosen. In this system, the charge ordering is a consequence of the dz^2-orbital order. Recent experiments using high-temperature powder diffraction have shown that the local octahedral distortions around the Jahn-Teller ions (M1 sites) are conserved up to 800 K, as well as the orderliness of the arrangement of these octahedra. The elongated axial Mn1-O bond lengths are stacked in double chains, leading to the ordering of strains and a periodicity of charge distribution. The Mn^{3+} electron lattice is expected to be strongly pinned on a crystal lattice. This leads to a gain in the electrostatic energy in the case of the Mn^{3+} ions located at "preferred" M1 sites. Therefore, Mn_2BO_4, allowing both di- and trivalent substitution, is a good model system with which one can trace the long-range order origination.

Recently, the heterometallic warwickite system $Mn_{2-x}Fe_xBO_4$ (x = 0.3, 0.5 or 0.7) has been comprehensively studied using X-ray diffraction, X-ray absorption (XANES/EXAFS), Mössbauer spectroscopy, heat capacity and magnetic measurements [24,25]. The orthorhombic structure (*Pnam*) is found for all samples. The substitution of Mn^{3+} ions for Fe^{3+} ions with close ionic radii, $r_i(Mn^{3+}) = r_i(Fe^{3+})$ = 0.645 Å according to Shannon [26], induces the breakage of the long-range magnetic order and the onset of the short-range order AF correlations, which are enhanced with increasing Fe content. As a result, the spin-glass transition was observed below T_{SG} = 11–17 K, depending on the Fe concentration. Mössbauer spectroscopy measurements have shown that the Fe^{3+} ions in the high-spin state are distributed over two metal sites, thereby causing cation disorder. Here, we focus on the $Mn^{2+}_{1-x}Mg^{2+}_xMn^{3+}BO_4$ ($0.0 < x < 1.0$) warwickites, where the Jahn-Teller ions are preserved.

There are several known magnesium-based warwickites, including $MgTiBO_4$ [19], $MgVBO_4$ [9], $MgCrBO_4$ [9] and $MgFeBO_4$ [9,17,18], which show the transition to the spin-glass state at low temperatures. As seen from Fig. 2, the critical temperature monotonically increases with the spin value of the magnetic ion increasing. The $Mg_{0.76}Mn_{1.24}BO_4$ compound has already been reported by Norrestam [27], but its physical properties were hitherto unknown. Our recent work has revealed that the Mg-Mn warwickite system shows signs of the antiferromagnetic long range order below T_N = 16 K [28]. The present study investigates the effect of the divalent substitution Mn^{2+}-Mg^{2+} on the cation order, the charge states of the metal sites, the local octahedral distortions and the magnetic properties of $Mn_{2-x}Mg_xBO_4$ ($0.0 < x < 1.0$) solid solutions.

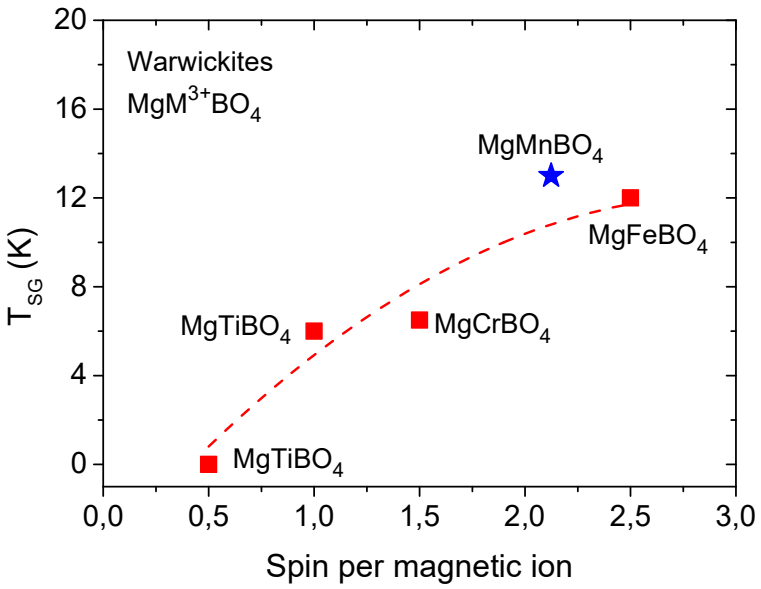

Fig. 2. Temperatures of magnetic transitions as a function of spin value in the magnesium warwickites $MgMBO_4$ (M = Ti^{3+}, V^{3+}, Cr^{3+}, Mn^{3+} or Fe^{3+}). The $MgMnBO_4$ warwickite only undergoes the antiferromagnetic transition while other materials show spin-glass transitions. The dashed line is a guide for the eye.

2. Experimental

Single crystals of $Mn_{2-x}Mg_xBO_4$ solid solutions were obtained using flux synthesis from the system $(100–n)\%mass.(Bi_2Mo_3O_{12} + p\cdot B_2O_3 + q\cdot Na_2O) + n\%mass.(x^*\cdot MgO + 0.5\cdot(2-x^*)\cdot Mn_2O_3 + 0.5\cdot B_2O_3)$. The magnesium oxide content (x^*), q and p coefficients and concentration n are shown in Table 1. The fluxes for each x^* and the corresponding parameters of the flux system were prepared in a platinum crucible (V = 100 cm^3) at a temperature of 1100 °C by sequential melting of powder mixtures: first, $Bi_2Mo_3O_{12}$ and B_2O_3, then Mn_2O_3 and MgO, and finally, the powder of Na_2CO_3 added in portions. The high-temperature crystallising phase in a sufficiently wide temperature range (no less than 40 °C) was the $Mn_{2-x^*}Mg_{x^*}BO_4$ warwickite phase. The saturation temperatures of fluxes depending on the concentration x^* are presented in Table 1.

Table 1. Parameters of fluxes: magnesium concentration (x^* is the target concentration), crystal-forming oxide concentration (n), weight coefficients – concentration of the boron and sodium oxides (p and q, respectively) and saturation temperatures (T_{sat}).

x^*	0.67	0.80	0.91
n, %	19.0	20.0	20.9
p	1.90	1.82	1.73
q	1.40	1.75	2.10
T_{sat}, °C	845	870	880

After the preparation process, the fluxes were homogenised at 1100 °C for 3 h. When the homogenisation is completed, the platinum crystal holder (rod) was inserted to the flux. Then, the temperature was first rapidly reduced to T_{sat}-10 °C and then slowly reduced at a rate of 4 °C/day. In five days, the growth was completed, the crystal holder with single crystals was extracted from the flux. Grown single crystals, in a shape of black prisms in a length up to 5 mm and the cross-section size up to 0.4×0.4 mm^2, were separated from the crystal holder and flux remainder by etching in a 20% solution of nitric acid. Single crystals of $Mn_{2-x^*}Mg_{x^*}BO_4$ with x^* = 0.67, 0.80 and 0.91 were obtained.

An X-ray crystallographic study was carried out with a SMART APEX II single crystal diffractometer (Bruker AXS, analytical equipment of Krasnoyarsk Centre of collective use of SB RAS) equipped with a PHOTON 2 CCD detector, graphite monochromator and Mo Kα radiation source. The structure was solved by direct methods [29] using the SHELXS program. The structural refinement was carried out by least-square minimisation in the SHELXL program [30] using anisotropic thermal parameters of all atoms. The main information regarding crystal data, data collection and refinement is reported in Table A1.

The *dc* magnetisation measurements were performed on single crystals using a Quantum Design PPMS in the temperature range of 2–300 K and an external magnetic field of 10 kOe. The magnetic field was applied parallel and perpendicular to the needle axis, which coincides with the *c* axis of the crystal. For the $Mn_{1.37}Mg_{0.63}BO_4$ composition, the magnetic measurements were carried out at low temperatures and high magnetic fields (±9 T).

The heat capacity as a function of temperature was measured on single crystals using the Quantum Design PPMS. The crystals were glued to the sample holder with Apiezon grease.

3. Results

3.1. Crystal structure

The symmetry and space group were found to be monoclinic and P121/n1 (No. 14), respectively, for all samples. With the magnesium concentration increase, the solid solutions were found to crystallise in the hulsite and orthopinakiolite structures. The atom coordinates, thermal parameters and selected interionic distances are listed in Tables A2–A4, respectively.

It is noteworthy that the Mg-Mn system under investigation shows cation ordering, where the Mg atoms have an evident tendency to occupy the M2 site. The magnesium atom distribution is almost independent of the Mg concentration and can be determined as Mg(1):Mg(2) = 0.1:0.9 (Fig. 3). We conclude that the isovalent substitution $Mn^{2+}\rightarrow Mg^{2+}$ does not induce remarkable cationic disorder as established for other heterometallic warwickites.

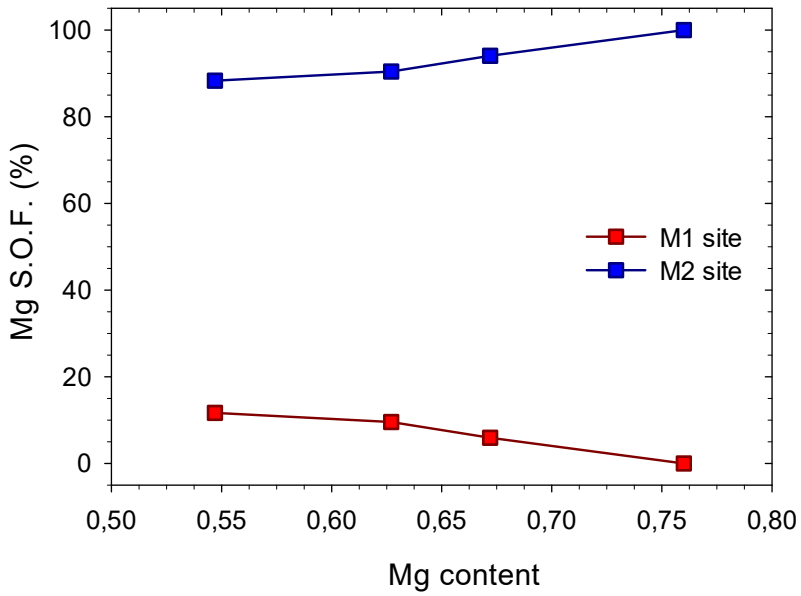

Fig. 3. Magnesium site occupation factor (SOF) as a function of Mg content in $Mn_{2-x}Mg_xBO_4$ solid solutions, where the Mg content is extracted from XRD data. The data for $x = 0.76$ are taken from the original work [27].

Figure 4 shows the dependencies of the lattice parameters of the $Mn_{2-x}Mg_xBO_4$ solid solutions versus the Mg concentration along with the data for Mn_2BO_4 [21] and $Mn_{1.24}Mg_{0.76}BO_4$ [27]. One can see that the cell parameters *b* and *c* decrease with increasing in Mg content, while the *a* parameter and angle β demonstrate non-monotonous behaviour. Such non-monotonous behaviour can be explained from the point of view of the change in the crystal structure distortions. Two main sources could be highlighted: 1) the difference in the size of the lattice sites, which is related with the difference in the ionic radii of the isomorphically substituting metals; 2) the peculiarities of the electronic structure of the ions (Jahn-Teller effect). The presented data show a steady decrease of the parameters, including volume, under the reduction of the cation size (r_i = 0.83 Å for Mn^{2+} and 0.72 Å for Mg^{2+}) to $x_c = 0.76$ [27]. Above this concentration, the change of the monoclinic distortions occurs, which manifests itself in the change of space group from P121/n1 to P121/a1.

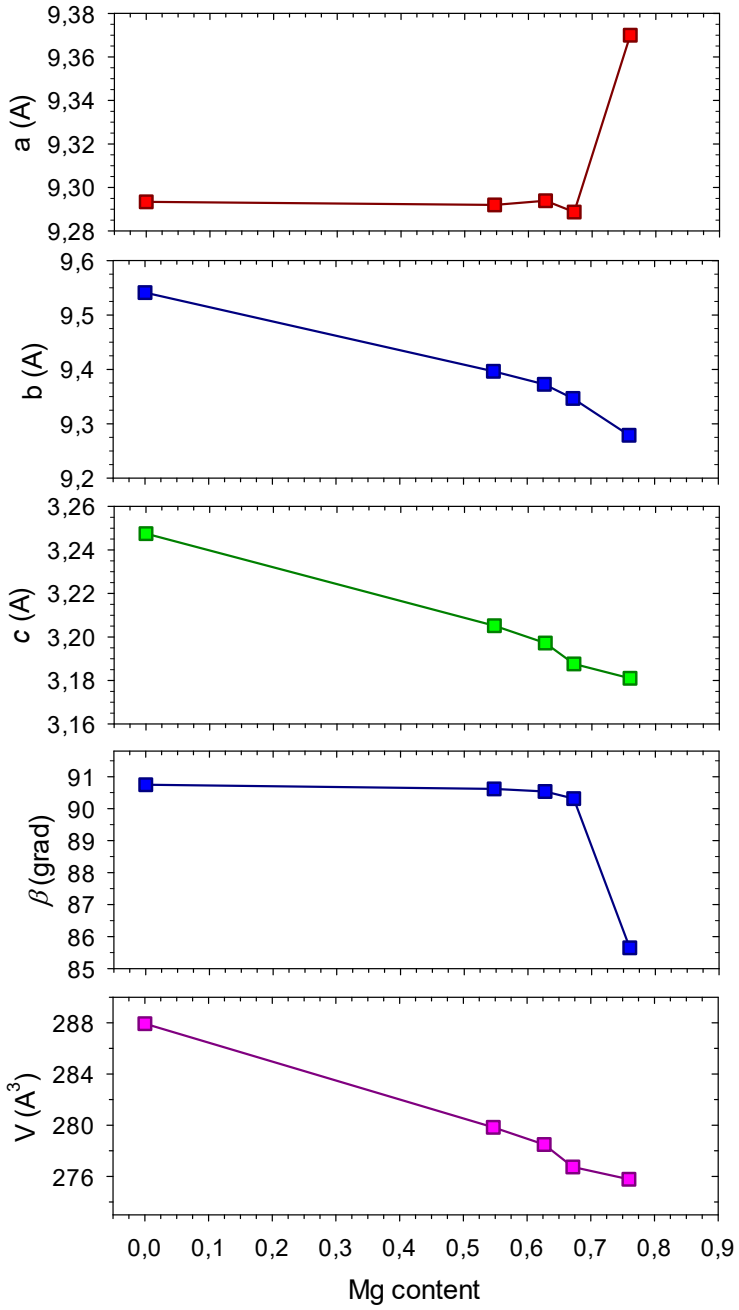

Fig. 4. Lattice parameters and volume of $Mn_{2-x}Mg_xBO_4$ solid solutions with varying Mg content. The errors are smaller than the symbol size. Hereinafter, we use the crystal data for x = 0.0 and 0.76 obtained from Refs. [21] and [27], respectively.

To evaluate the oxidation states of Mn and Mg ions, a bond-valence-sum approach was applied [31]. The results are shown in Fig. 5(a). It can be clearly seen that the M1 site is occupied by the manganese ions with the oxidation state 3+, while the M2 site is filled by the mixture of Mg^{2+} and Mn^{2+} ions. When the concentration increases, the effective charge of Mn ions at the M2 site shows an increment. It nevertheless has an exclusive size effect and is caused by the reduction in the interionic distances <M2-O> due to the substitution of Mn^{2+} ions by the smaller Mg^{2+} ions (Fig. 5(b)). The average valence state of metal ions at the M2 site, accounting

for the S.O.F., is found to be close to 2+. This result suggests that in the $Mn_{2-x}Mg_xBO_4$ solid solutions, the charge distribution over two non-equivalent metal sites has periodical character when the M1 position is occupied by only the trivalent ions and the M2 position is occupied by only the divalent ions. Such a situation does not occur in other heterometallic warwickites, which demonstrate a rather small difference in the charges of two metal sites (see below). The presence of charge ordering in Mn-Mg warwickites is probably caused by the strong electron-phonon coupling arising due to the local $M1O_6$ oxygen octahedral distortion.

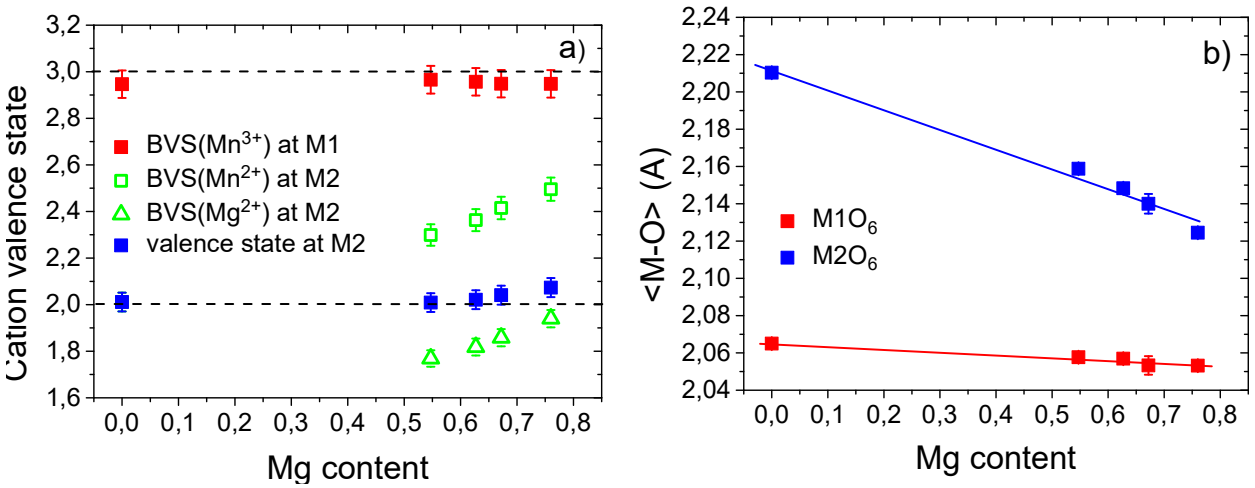

Fig. 5. a) Cation valence states at M1 and M2 sites as a function of the Mg content in $Mn_{2-x}Mg_xBO_4$. The dotted lines mark di- and trivalent cation states. b) Concentration dependences of the mean octahedral bond-lengths <M-O>. The straight lines represent guides for the eye.

As follows from crystal chemical principles, the transition metal ions prefer more distorted sites due to the energy gain of crystal field stabilisation. In the case of Mn^{3+} ions, the fivefold degenerated *d*-level splits into a threefold degenerated t_{2g}-level and a twofold degenerated e_g-level under the action of the crystalline field. This configuration of the degenerated orbitals is unstable and strong electron-phonon coupling arises. The electron-phonon coupling reduces the energy of the degenerated system by the lattice deformation and the lowering of its symmetry. This is accompanied by the local stretching along one of the octahedral axes and the simultaneous compression along the two others (Jahn-Teller theorem). In Mn_2BO_4, the $M1O_6$ octahedra have strong elongation along the O1-M1-O3 axes (axial bond), while the other four bonds (equatorial) are short. The Mg^{2+} substitution triggers the progressive compression of the axial bond and the simultaneous stretching of the equatorial bonds of $M1O_6$ octahedra (Fig. 6(a)). One can suggest that the observed deformation of $M1O_6$ leads to the reduction of e_g- and t_{2g}-levels splitting and, hence, to an increase in the stabilisation energy. In such a case, the energy gain can be obtained by the increase in the local octahedral distortions, typical for Mn^{3+} ions.

This possibly occurred for the composition with x = 0.76 and manifested itself in the axial and equatorial bond changes.

As for $M2O_6$, for x = 0, this octahedron is compressed along the axial bond (O2-M2-O4) and has significant stretching in the equatorial plane. With the magnesium concentration increasing, the $M2O_6$ octahedron undergoes compression of all bond lengths (Fig. 6(b)). A rapid shortening of the equatorial bond lengths results in a change of the direction of the main octahedral axis. The direction of the main octahedral axis is changed, as shown in Figs. 6(c) and (d) for $x \leq 0.67$ and $x \geq 0.76$, respectively. The Mg substitution induces the changes in the local octahedral distortions of both metal sites, but mainly the M2 site, leading to the changes of the long-range monoclinic distortions reflecting in the P121/n1 → P121/a1 transformation.

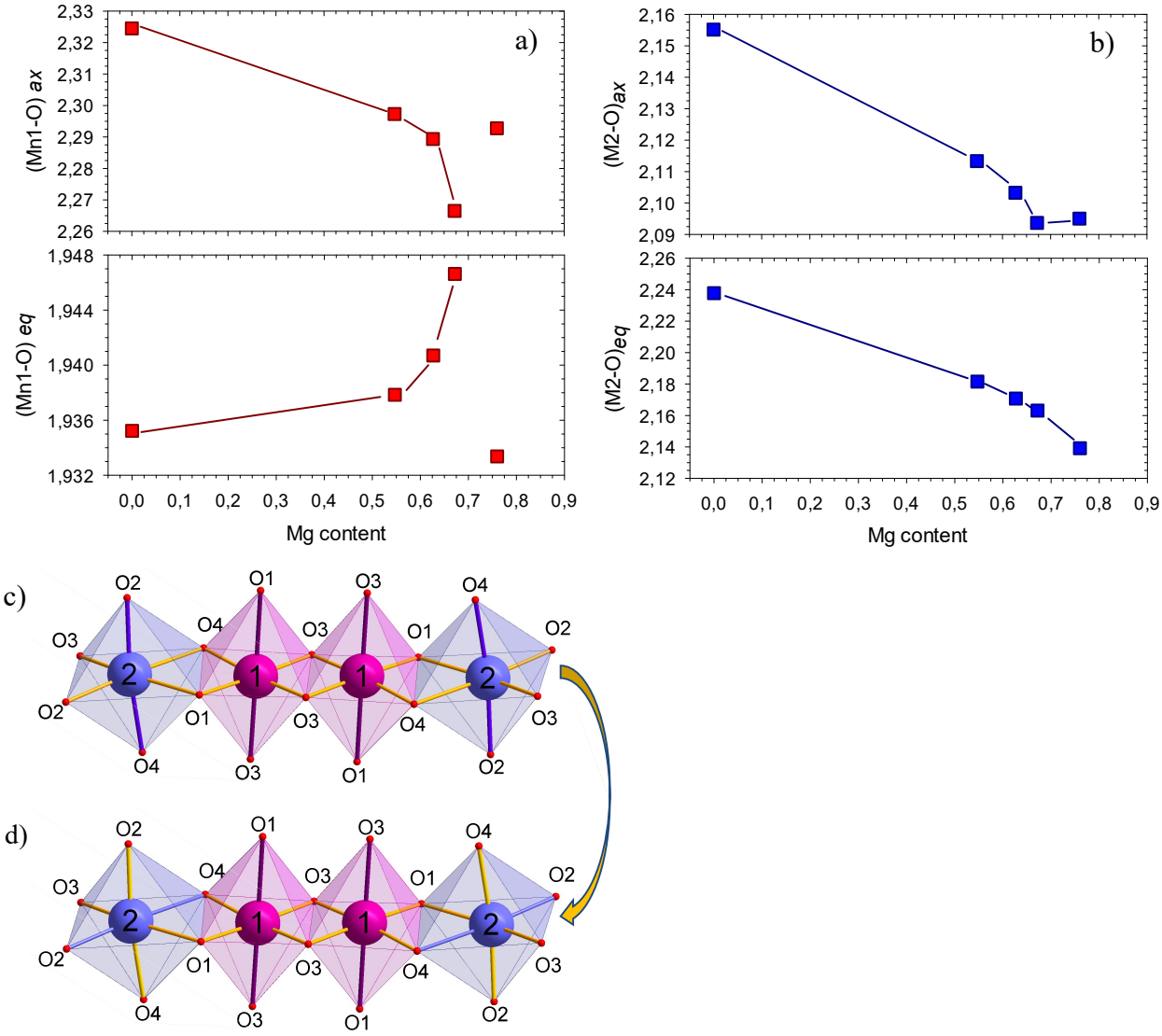

Fig. 6. Axial and equatorial bond lengths in $M1O_6$ (a) and $M2O_6$ (b) octahedra as a function of Mg content in $Mn_{2-x}Mg_xBO_4$ warwickites. c) and d) Arrow shows the change in the direction of the main octahedral axis at the M2 site for $x \leq 0.67$ and $x \geq 0.76$.

3.2. *Magnetisation*

Field-cooled (FC) and zero-field-cooled (ZFC) *dc* magnetisation measurements were performed on a single crystal with an applied field of 10 kOe at different directions of the applied magnetic field relative crystallographic *c* axis. Figure 7 shows the temperature dependence of the magnetic susceptibility of three compounds $Mn_{2-x}Mg_xBO_4$ at the applied field parallel to the *c* axis based on the FC magnetisation data. A sharp cusp in the temperature dependence of the magnetic susceptibility is shown. The critical temperatures are T_N = 16, 14 and 13 K for x = 0.55, 0.63 and 0.67, respectively. Down to the lowest temperatures, the FC and ZFC curves do not diverge (inset of Fig. 7). It is noteworthy that the irreversibility of the FC/ZFC magnetisation is characteristic behaviour in spin-glass systems and was observed in other heterometallic warwickites, such as $MgFeBO_4$, $Mn_{2-x}Fe_xBO_4$, $Mg_{1-x}Co_xBO_4$ [17, 24].

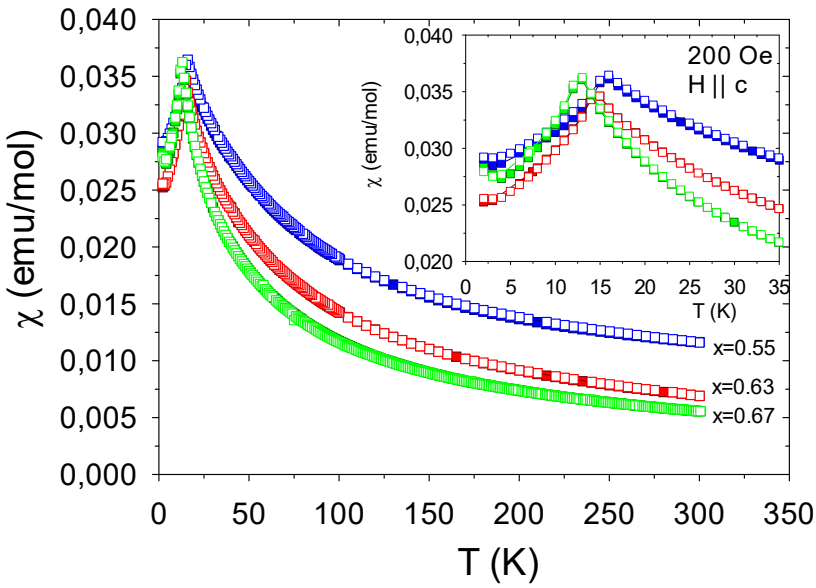

Fig. 7. Temperature dependences of magnetic susceptibility of $Mn_{2-x}Mg_xBO_4$ measured under a magnetic field of 200 Oe applied parallel to the *c* axis. The inset shows the ZFC (filled squares) and FC (empty squares) curves near the T_N.

The magnetic anisotropy was found to be small for all three Mn-Mg warwickites, as can be observed from Fig. 8, where the magnetic data for x = 0.67 are drawn as an example. The *c* axis seems to be a hard magnetisation direction that is similar to Mn_2BO_4 [21] and $CoFeBO_4$ [17]. Below T_N, the FC magnetisation perpendicular to the *c* axis increases. The linear behaviour above 150 K indicates that the susceptibility obeys the Curie–Weiss law. In Table 2, the Weiss temperature and an effective magnetic moment are listed for both orientations for all samples.

Assuming a high-spin state for all manganese ions, the magnetic moment per formula unit can be calculated as follows:

$\mu_{eff} = \sqrt{(1-x)\cdot g^2 \cdot S_{Mn^{2+}} \cdot (S_{Mn^{2+}}+1) + g^2 \cdot S_{Mn^{3+}} \cdot (S_{Mn^{3+}}+1)}$, where $S_{Mn^{2+}}$ = 5/2, $S_{Mn^{3+}}$ = 2, g = 2 for spin magnetism only (the last column in Table 2).

Several interesting conclusions can be drawn from these measurements:

(1) The effective magnetic moment decrease in the row of the samples x = 0.55, 0.63 and 0.67, in agreement with the diamagnetic substitution Mn^{2+} - Mg^{2+}.

(2) The values of $\mu_{eff}^{\perp}$ and $\mu_{eff}^{\parallel}$ indicate the magnetic anisotropy in the paramagnetic regime.

(3) The average magnetic moment calculated as $\mu_{eff}^{av} = \sqrt{\frac{2\cdot(\mu_{eff}^{\perp})^2+(\mu_{eff}^{\parallel})^2}{3}}$ gives effective spin moments much lower than those expected for all samples.

(4) The Weiss temperature is estimated to be negative for all samples. Note that the diamagnetic substitution induces the enhancement of the nearest-neighbour antiferromagnetic interaction reflecting in the gradual increasing in Weiss temperature and points to a rather strong magnetic interaction between Mn^{3+} ions.

(5) The substitution of the diamagnetic Mg^{2+} instead of magnetic Mn^{2+} led to a monotonic decrease in the Neel temperature.

A tentative interpretation of the low effective magnetic moment for $Mn_{2-x}Mg_xBO_4$ can be given as follows. Although the high-temperature interval of 150–300 K can be used to fit a straight line with high accuracy (the linearity coefficient R = 0.999), it is possible that the extension of the data to higher temperatures will yield an effective moment closer to the spin-only value. That is a complete paramagnetic state has not yet been reached, probably a somewhat degree of short-range order remains. Another possible explanation is there is a contribution of excited states to the average moment of the magnetic ions due to the unusual site symmetries in this structure.

The magnetisation curves below T_N exhibit straight lines characteristic of the AFM order. In Fig. 9, the magnetisation curves for all samples are presented.

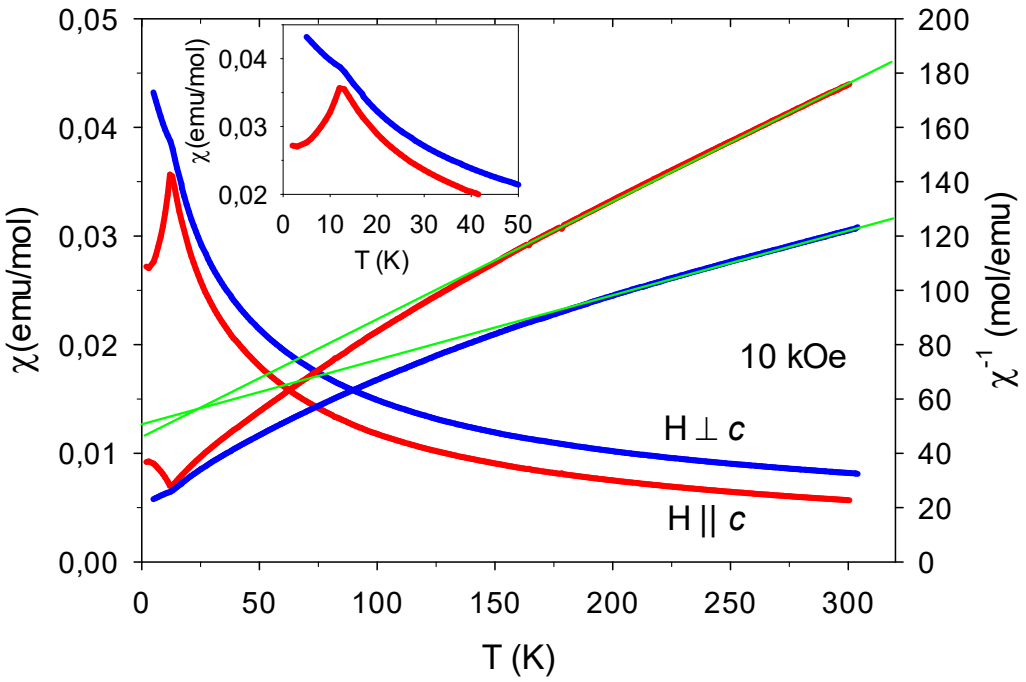

Fig. 8. FC magnetisations measured with an external magnetic field parallel and perpendicular to the *c* axis for $Mn_{1.33}Mg_{0.67}BO_4$. The inset shows the magnetic behaviour near the critical transition temperature.

Table 2. Magnetic parameters for $Mn_{2-x}Mg_xBO_4$ warwickite system.

	T_N (K)	$\theta^{\parallel}$ (K)	$\mu_{eff}^{\parallel}$ (μ_B/f.u.)	$\theta^{\perp}$ (K)	$\mu_{eff}^{\perp}$ (μ_B/f.u.)	μ_{eff}^{av} (μ_B/f.u.)	μ_{eff} (μ_B/f.u.)
Mn_2BO_4 [21]	26	-118	6.25	-134	6.95	6.72	7.68
$Mn_{1.45}Mg_{0.55}BO_4$	16	-79	4.67	-146	6.05	5.63	6.30
$Mn_{1.37}Mg_{0.63}BO_4$	14	-109	4.79	-202	6.19	5.76	6.08
$Mn_{1.33}Mg_{0.67}BO_4$	13	-114	4.33	-213	5.79	5.35	5.96

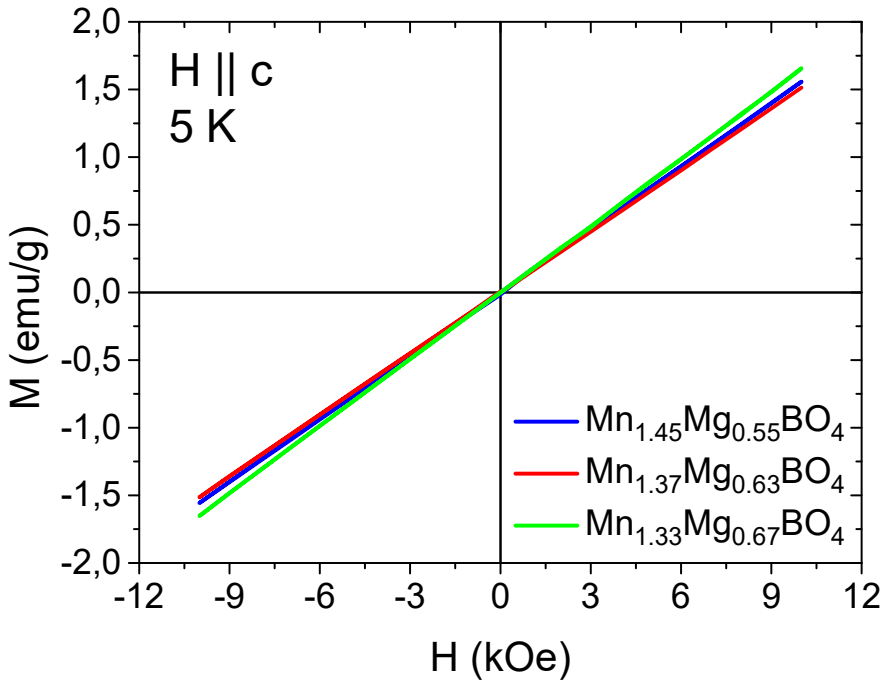

Fig. 9. Magnetisation curves of $Mn_{2-x}Mg_xBO_4$ warwickites measured at T = 5 K. The applied magnetic field is parallel to the c axis.

3.3. Heat capacity

The evidence for antiferromagnetic transitions is obtained from the heat capacity measurements (Fig. 10). The temperature dependence of the molar heat capacity for all samples demonstrates well-resolved lambda points at T_N = 14, 13 and 12 K for x = 0.55, 0.63, and 0.67, respectively.

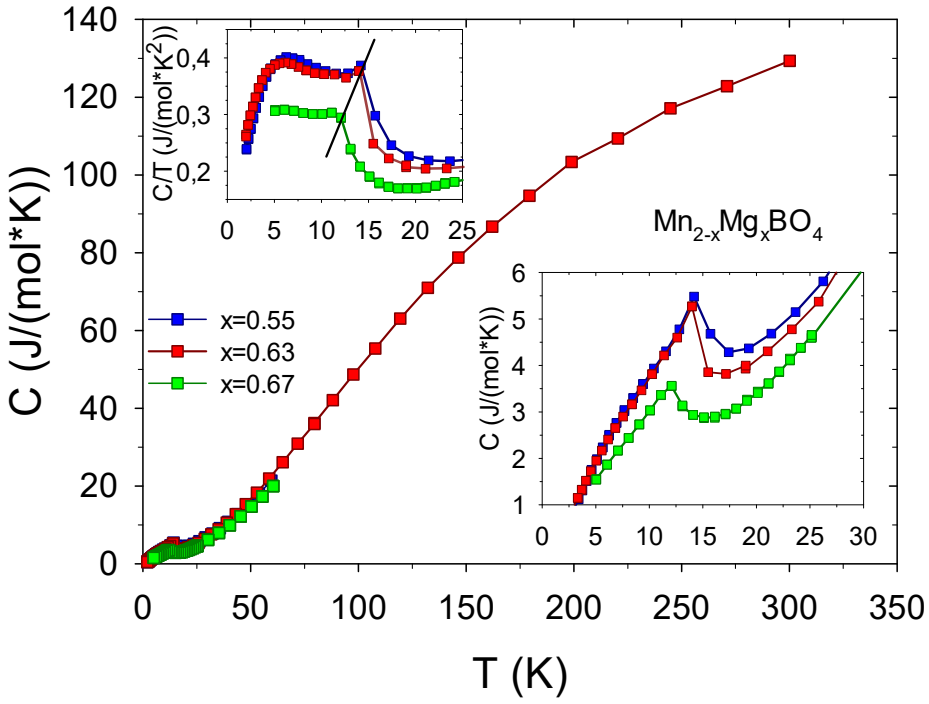

Fig. 10. Temperature dependences of the heat capacity measured at zero magnetic field for $Mn_{2-x}Mg_xBO_4$ warwickites. Top inset: specific heat plotted as C/T vs. T. The straight line shows the shift of T_N with Mg concentration. Bottom inset: the lambda point anomalies observed at the critical temperatures T_N.

3.4. High-field magnetisation of Mg-Mn heterometallic warwickites

To complement our studies on Mg-Mn warwickites, we have carried out isothermal magnetisation experiments at low temperatures, in order to better elucidate their ground-state properties. The measurements were performed for $Mn_{1.37}Mg_{0.63}BO_4$. Magnetic characterisation for one sample with a mass of 1.13 mg oriented perpendicular to H and three samples with a mass of 2.41 mg oriented parallel to H were carried out.

Figures 11(a) and (b) show the field dependences of magnetisation at 4.2, 10, 12, 16 and 30 K for H||c and H⊥c, respectively. All curves demonstrate a rapid linear rise. However, for H||c,

this trend is followed by an abrupt increase of the magnetisation above H_{C1} = 35 kOe (at 4.2 K). Above H_{C2} = 64 kOe, the magnetisation again shows linear behaviour with a larger value of slope. This can be more clearly seen from the *d*M/*d*H plot (inset to Fig. 11(a)). The appearance of the peaks in *d*M/*d*H is an indication of a spin-flop transition. With increasing temperatures, this feature is weakened and disappears at 16 K. The peak position of *d*M/*d*H decreases from H_{SF} = 61 kOe at 4.2 K to 33 kOe at 12 K. Field-sweep experiments at 4.2 K showed that the spin-flop appears at slightly different magnetic fields when the magnetic field increases and decreases, suggesting the existence of a small magnetic anisotropy. For H ⊥ c, the magnetisation shows typical antiferromagnetic behaviour and M⊥ increases linearly with H up to H_{C1}, showing the deviation from linearity above this field.

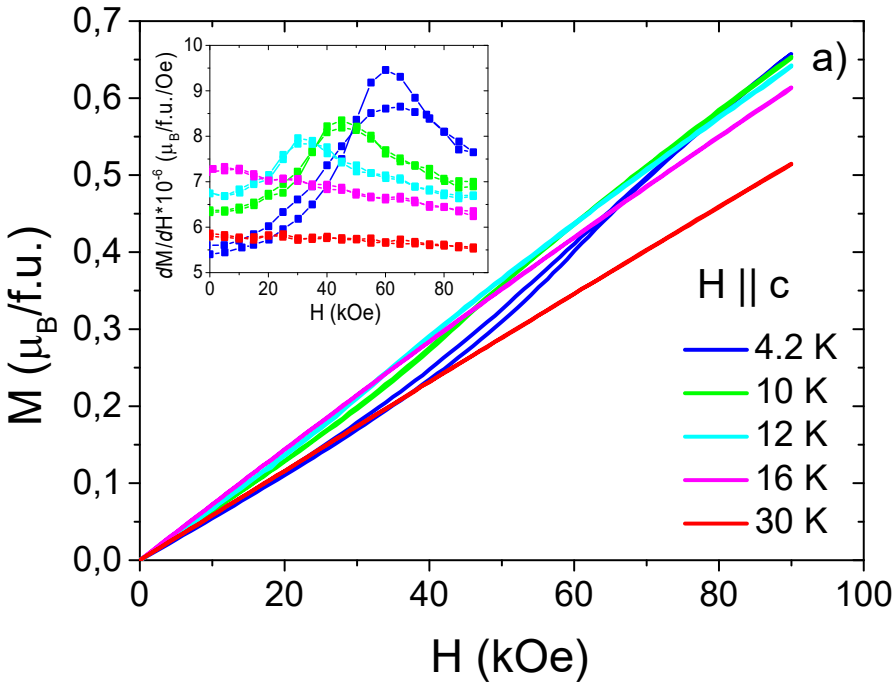

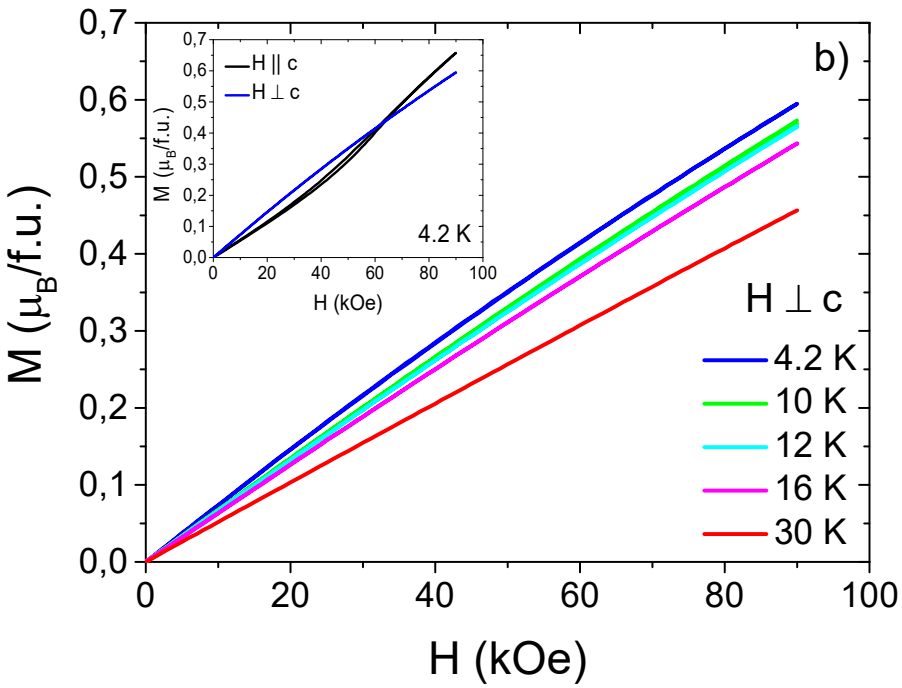

Fig. 11. Magnetisation isotherms for $Mn_{1.37}Mg_{0.63}BO_4$ measured with magnetic fields applied parallel (a) and perpendicular (b) to the *c* axis. The inset to (a) is the derivatives *d*M/*d*H at various temperatures, revealing the decreasing of the spin-flop field with temperature. The inset to (b) shows the changing of the magnetic anisotropy from easy-plane to easy axis at H_{C2} = 64 kOe.

The magnitudes of the initial susceptibilities (H < H_{SF}) are $\chi_\perp$ = 7.34·10^{-6} μ_B/f.u./Oe and $\chi_\parallel$ = 5.45·10^{-6} μ_B/f.u./Oe for the perpendicular and parallel directions of the external field, respectively. The small anisotropy of the magnetic response suggests that the ordered magnetic moments of Mn ions have both in-plane and out-of-plane components. The extrapolation to zero field of the $M_\parallel$ data in high fields has a negative intercept to the magnetisation axis, suggesting the net moment is generated during the phase transition. The spin-flop transition can be further analysed by subtracting the linear contribution (antiferromagnetic component) shown as a dashed line in Fig. 12. Above H_{C1}, the magnetic moment ΔM undergoes the reorientation process, to be parallel to the applied field, which allows an additional contribution to the total magnetisation along the *c* axis. The magnitude of the increased magnetic moment ΔM = 0.017 μ_B/f.u. at 4.2 K and gradually decreases as the temperature increases (inset to Fig. 12). Note that the end member Mn_2BO_4 shows the spin-flop transition at H_{SF} = 24 kOe when the external field is applied perpendicular to the *c* axis. Different from MgMn, the extrapolation of magnetisation of MnMn in the high fields goes straight across the origin, suggesting no net moment appears at the transition. The fact that the magnetic susceptibility of the MgMn sample is very close to that found for MnMn ($\chi_\perp$ (4.2 K) = 4.02·10^{-6} μ_B/f.u./Oe), reflecting that at low temperatures, the

antiferromagnetic interactions prevail, leading to antiparallel alignment of the manganese magnetic moment and hence, to antiferromagnetic ordering.

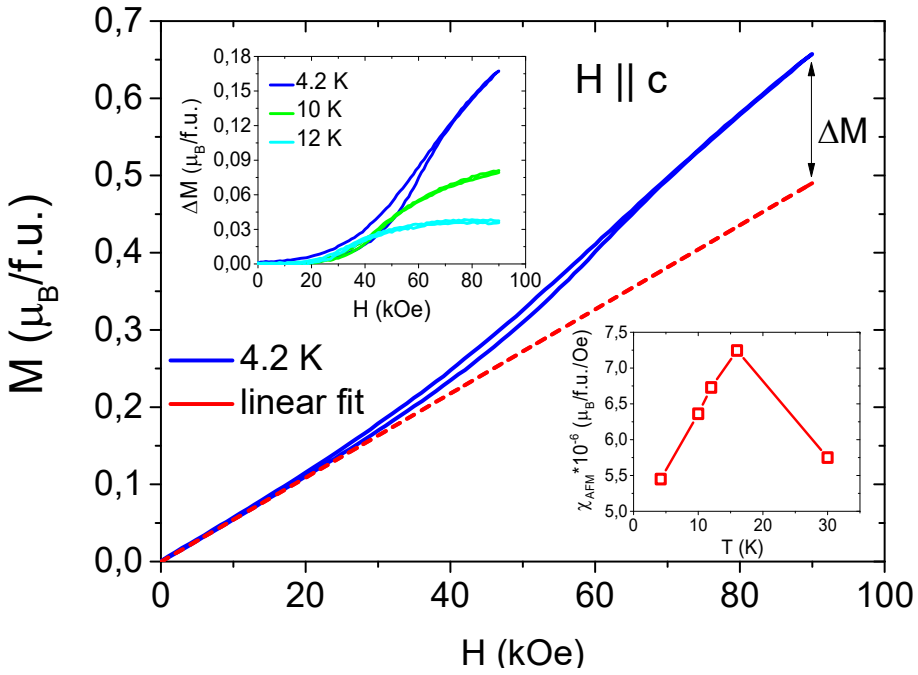

Fig. 12. Magnetisation isotherm at 4.2 K for single crystal $Mn_{1.37}Mg_{0.63}BO_4$ measured with an applied magnetic field along the *c* axis. The top inset shows a magnetic moment ΔM obtained by subtracting linear dependence (dashed line) from the raw data. The bottom inset is a temperature dependence of the antiferromagnetic susceptibility, determined at the low-field range (H<Hc). The maximum of $\chi_{AFM}(T)$ curve occurs near to $T_N = 14$ K.

The observed spin-flop transition in MgMn can be rationalised by adopting the concept of several interpenetrating sublattices, usually employed to describe antiferromagnets where each sublattice consists of the chains of magnetic ions. The diamagnetic substitution of Mn^{2+} ions by Mg^{2+} ions leads to the weakening of the exchange interactions both Mn^{2+}-Mn^{2+} and Mn^{3+}-Mn^{2+}. A sufficient external field H_{C2} overwhelms the weak AF interactions and causes the reorientation process of the weakly-coupled magnetic component. As a result, there occurs the change of the magnetic anisotropy from easy-plane (*ab* plane) for $H<H_{C2}$ to easy-axis (*c* axis) for $H>H_{C2}$.

The obtained magnetic data of the $Mn_{1.37}Mg_{0.63}BO_4$ sample can be summarised as follows. The magnetic interaction between manganese ions is antiferromagnetic, resulting in the antiparallel alignment. The AFM, SF and PM states were observed under certain conditions. The phase transition from PM to the long-range AFM state with $T_N = 14$ K regardless of the external magnetic field. At $T<T_N$, the low field and temperature stabilise the AFM phase, while the high field and temperature causes the SF phase. The complete magnetic characterisation allows building the magnetic phase diagram (Fig. 13).

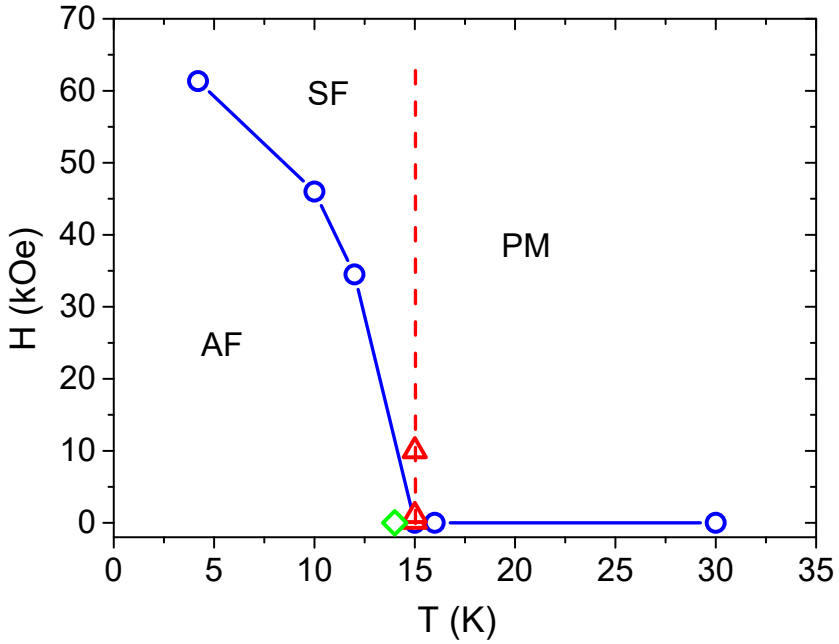

Fig. 13. Magnetic phase diagrams for $Mn_{1.37}Mg_{0.63}BO_4$ warwickite. The blue circles are data obtained from the M(H) curves, the red triangles are from the χ_{dc}(T) curves and the green diamond is from C_p(T) curve. The solid and dotted lines are a guide to the eye.

4. Discussion

In Mn_2BO_4, the charge ordering of type Mn^{2+}(2)-Mn^{3+}(1) results from the preferential occupation of the $3d_z^2$ orbitals on the Mn^{3+} ion. The lowering of the symmetry from the orthorhombic (Pnma) warwickite structure to the monoclinic (P121/n1) occurs through the cooperative Jahn-Teller distortions to minimise the elastic energy. The same distortions, but decreasing in strength, are present in the solid solutions of $Mn_{2-x}Mg_xBO_4$ showing a monoclinic structure, isomorphous to the structure of Mn_2BO_4. This behaviour reflects strong electro-phonon coupling of Mn^{3+} ions, which are prone to occupying the M1 site in the $Mn_{2-x}Mg_xBO_4$ system. In $Mn_{2-x}Fe_xBO_4$ warwickites, the Fe^{3+} is not a J-T ion and prefers a fairly symmetric coordination environment. This conformation disrupts the simultaneous formation of both long and short bonds at a given site, thereby reducing the stabilisation of the local distortions. The octahedrally symmetric Fe^{3+} and the J-T active Mn^{3+} ions are disordered over crystallographic sites, rather, it is more likely that J-T distortions are present locally but the orientation of these distortions is disordered. This leads to the inability to develop the long-range ordered pattern of occupied orbitals. The disappearance of the orbital order causes the break of the charge ordering. The random cation distribution is the reason for magnetic disorder [17,24]. From Fig. 14, it is clear

that both substituted systems $Mn_{2-x}Mg_xBO_4$ and $Mn_{2-x}Fe_xBO_4$ undergo magnetic transitions with close values of the critical temperatures which are, however, quite different in nature.

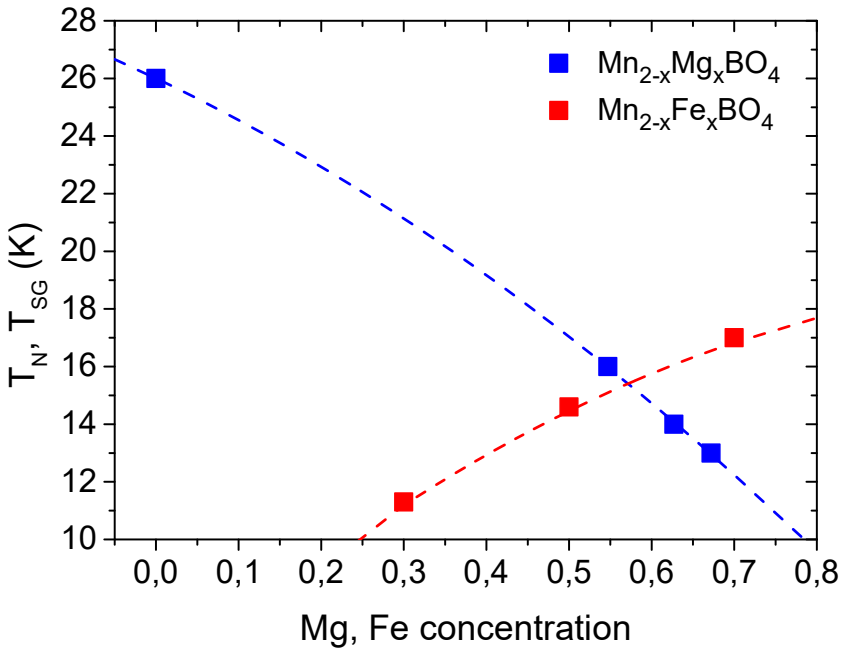

Fig. 14. Magnetic critical temperature as a function of the concentration for the warwickite systems $Mn_{2-x}Mg_xBO_4$ and $Mn_{2-x}Fe_xBO_4$.The dashed lines are guides for the eye.

Finally, we discuss the prerequisites for the occurrence of cation ordering in heterometallic warwickites. In this sense, magnesium-based warwickites $MgMBO_4$, where M is a trivalent metal ion, are promising systems in which to search for cation order, since Mg^{2+} allows us to study the size and the octahedral distortion effects of the M ion when the latter is varied. The known experimental studies give not numerous structural data on the $MgMBO_4$ warwickite, where M = Ti^{3+} [32], V^{3+} [12], Fe^{3+} [33], Sc^{3+} [27], Ga^{3+} [34], In^{3+} [35], Ta^{5+} [36] and Nb^{5+} [36]. In order to quantify the match of Mg^{2+} and M^{3+} ions to the cation order, we used two main parameters: the charge difference between two metal sites M1 and M2 (ΔCD) and the octahedral distortion parameter (Δ). The former depends on the cation distribution over non-equivalent sites and directly reflects the cation order. There exist two end cases corresponding to a completely random distribution (ΔCD equals zero) and completely ordered distribution (ΔCD equals unity). A quantitative measure of the magnitude of the local distortion is given by the octahedral distortion parameter $\Delta = \frac{1}{6}\sum_{i=1,6}\left[\frac{d_i - d}{d}\right]^2$, where d_i is an individual M-O bond-length and d is a mean <M-O>.

Several magnesium warwickites were collected from the literature. Only these compounds were chosen for which crystal structure analyses were available. The data are shown in Figs. 15 and 16. Continuing from $MgGaBO_4$ to $MgInBO_4$, the difference in the ionic radii of metal ions

actually increases (r_{Ga}^{3+} = 0.620, r_{V}^{3+} = 0.640, r_{Sc}^{3+} = 0.745 and r_{In}^{3+} = 0.800 Å), yet the character of the cation distribution is preserved. In contrast, for the Fe^{3+}, V^{3+}, Ta^{5+}, Nb^{5+} and Mn^{3+} ions with close ionic radii, the situation is varied from almost cation disordered ΔCD ~0.1 v.u. (for MgFe) to a high degree of cation order ΔCD ~0.9 v.u. (for MgMn, MgTa and MgNb). All considered warwickites exhibit the distortion of the $M1O_6$ octahedron, a much larger distortion than that $M2O_6$ (Fig. 16). Another interesting observation is that the local octahedral distortions have two well-separated ranges. For octahedral site M1 (inner column of the ribbon), these are $\Delta(M1)<2.0\cdot10^{-3}$ and $\Delta(M1)>4.5\cdot10^{-3}$, while for the M2 site (outer column), these are $\Delta(M2)<1.5\cdot10^{-3}$ and $\Delta(M2)>2.0\cdot10^{-3}$. It is obvious the hetero-metallic warwickites MgMn, MgTa, MgNb exhibiting the cation order show a highest distortion parameter Δ. While the cation-disordered compounds tend to have a lower distortion parameter for both metal sites. Therefore, there is interrelation between the cation order and local octahedral distortion. The latter can also be enhanced by chemical pressure induced by oversized M^{3+} ions, as demonstrated by the behaviour of $MgInBO_4$ ($\Delta(M2) = 3.0\cdot10^{-3}$).

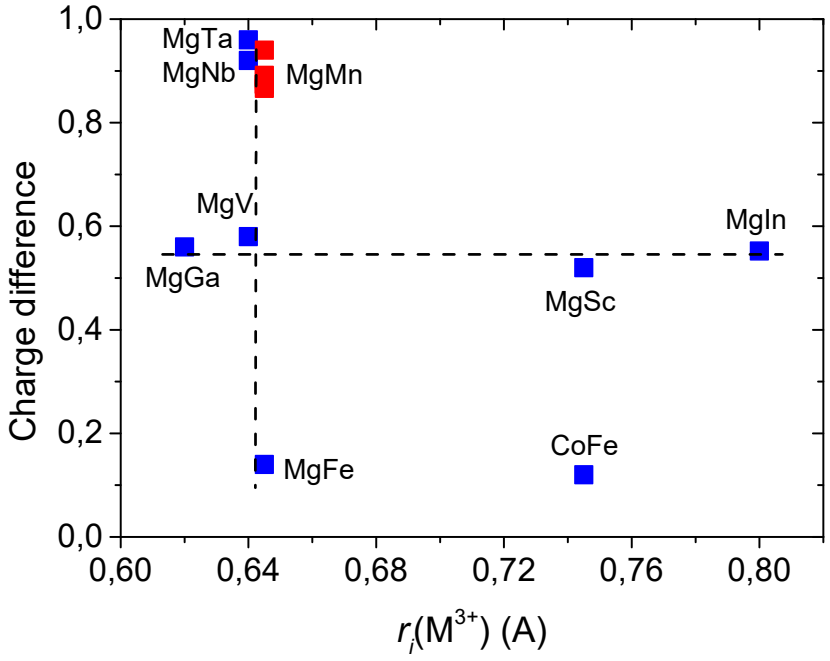

Fig. 15. Charge difference between two metal sites (v.u.) in the magnesium-containing warwickites. The available data for $CoFeBO_4$ are presented also.

Unlike the Mg-Mn warwickite, the compounds $Mg_5TaB_3O_{12}$ and $Mg_5NbB_3O_{12}$ have a strong driving force for the cation ordering as a result of the oxidation state difference of three between the Mg^{2+} and Ta^{5+}/Nb^{5+} ions. Additionally, these compounds exhibit a large octahedral distortions of $\Delta(M1) = 4.71\cdot10^{-3}$ and $6.23\cdot10^{-3}$ for Ta and Nb, respectively. Following the above assumption that the magnetic order is a consequence of the cation order and, hence a charge

order, one can expect an existence of long-range order in the heterometallic warwickites containing the pentavalent ions. We can therefore report that our preliminary results on the study of a novel cation-ordered warwickite $Co_5NbB_3O_{12}$ have confirmed this assumption [37].

The fact that the octahedral site cation ordering is influenced by the ordering of the local distortions is confirmed by the similar analysis performed for the homometallic compounds (they are also shown in Figs. 16). For V_2BO_4, only the room-temperature crystal structure data are available in the literature [23]. The high resolution synchrotron powder X-ray diffraction experiment revealed the orthorhombic symmetry (P*nma*, No.62). The sites V1 and V2 have similar <M-O> bond lengths and close values of distortion parameters. Nevertheless, the authors reported changes in the crystallographic symmetry upon cooling between 295 and 90 K, which is interpreted as the occurrence of the charge ordering at low temperatures. Fe_2BO_4 exhibits a much larger local distortions (ΔFe1 and ΔFe5) for the monoclinic phase (P1*c*1, No.7) ($T=100\ K < T_{CO}$) than that for the orthorhombic one (P*mnb*, No.62) ($T=355\ K > T_{CO}$) [38]. The transition to the charge ordering state is accompanied by the doubling of the *a*-parameter. With the higher symmetry, the even bond length distribution can be realised with tripling of the short crystallographic axis, as found in $Mg_5NbB_3O_{12}$ and $Mg_5TaB_3O_{12}$ [36] (Fig.17).

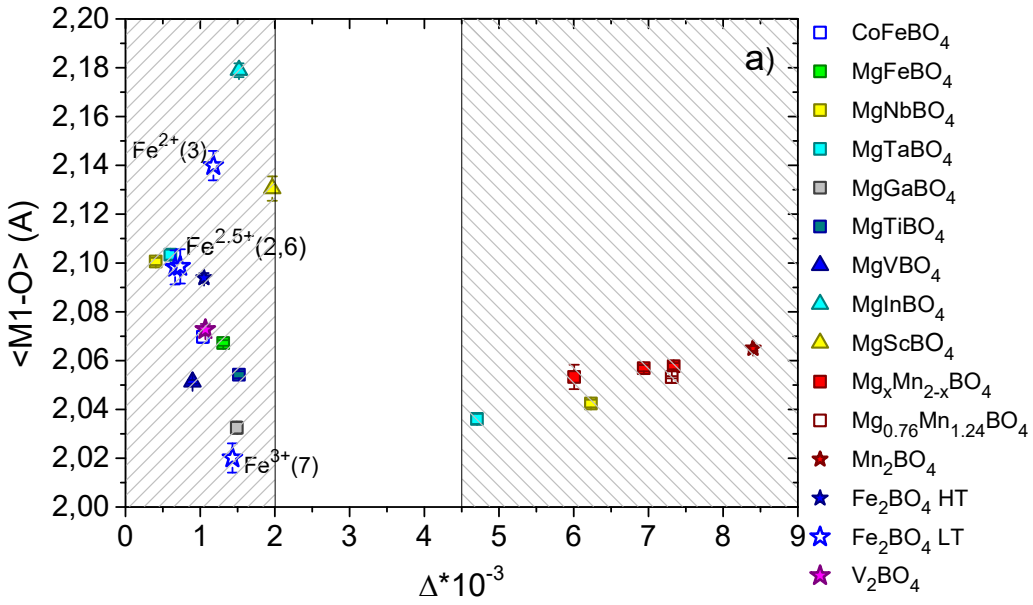

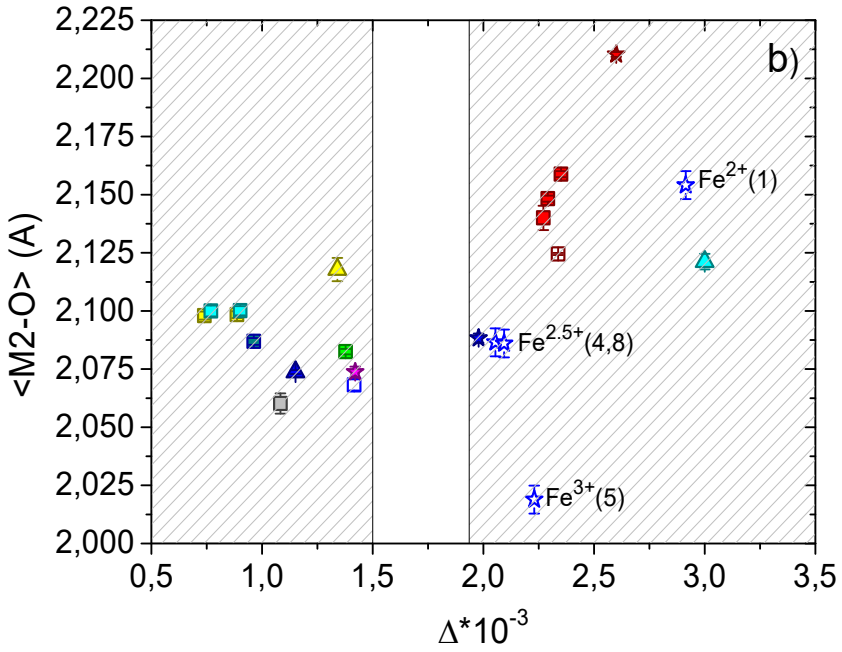

Fig. 16. Mean M-O bond lengths as a function of the distortion for $M1O_6$ (a) and $M2O_6$ (b) octahedra. The error-bars are taken from the original works.

From the above analysis, it is possible to draw the conclusion that the difference in the ionic radii is an insufficient factor for stabilising the cation order in the warwickites, but this lead to the idea that the local octahedral distortions is a key to the understanding of magnetic and electronic phenomena in these materials.

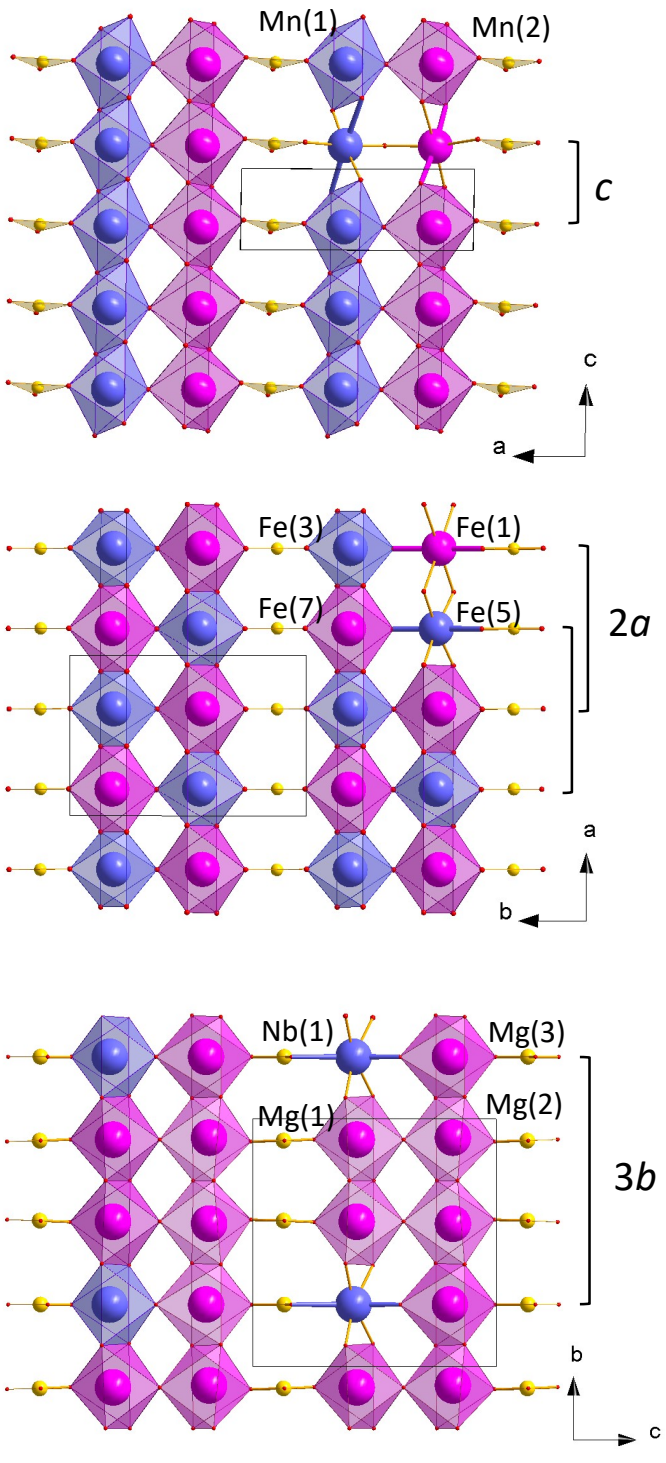

Mn_2BO_4
T=296 K
P121/n1(14) – monoclinic
a=9.2934(5) Å
b=9.5413(5) Å
c=3.2475(2) Å
β=90.751(1)°
V=287.93(3) Å^3
Z=2

Fe_2BO_4
T=100 K
P1c1(7) – monoclinic
a=6.3333 Å
b=9.3803 Å
c=9.2469 Å
β=90.0000°
V=549.34 Å^3
Z=8

$Mg_5NbB_3O_{12}$
T=298 K
Pnma(62) - orthorhombic
a=9.3682(3) Å
b=9.4344(2) Å
c=9.3379(3) Å
V=825.31(4) Å^3
Z=4

Fig. 17. The ordering of the local distortions in cation- and charge-ordered warwickites resulting in the doubling and tripling of the short crystallographic axis, as found in Mn_2BO_4 (a), Fe_2BO_4 (b), and $Mg_5NbB_3O_{12}$ (c). The double chains of metal ions separated by the (BO_3) groups form the planes shown in Fig. 1. The main axes of the octahedra, showing the largest distortion parameter are highlighted in bold.

4. Conclusion

In summary, we have investigated the structural, magnetic and thermodynamic properties of the heterometallic warwickites $Mn_{2-x}Mg_xBO_4$ with x = 0.55, 0.63 or 0.67. All samples were found to crystallise in a monoclinic P121/n1 symmetry similar to the end member Mn_2BO_4.

The lattice parameters display a monotonic change with the magnesium concentration. The local octahedral distortions associated with the Jahn-Teller effect of Mn^{3+} ions are persistent for all solid solutions, albeit reduced compared with that of Mn_2BO_4. A regular occupation of the M2 site by the Mg^{2+} ions was found in contrast with other heterometallic warwickites where cation disorder has a large effect. As a result, the charge distribution over two metal sites has a character of $Mn^{3+}(1)$ and $Mn^{2+}(2)/Mg^{2+}(2)$.

To the best of our knowledge, the $Mn_{2-x}Mg_xBO_4$ system is the first example of a heterometallic warwickite showing long-range order. Magnetic and thermodynamic measurements show that all samples undergo a transition from paramagnetic to an antiferromagnetic ordering state at the Neel temperatures T_N = 16, 14 and 12 K. The magnetic anisotropy is small with the c axis as an easy magnetisation direction at high fields. Careful investigation in the ordered state allows for the building of a magnetic phase diagram.

The next important finding is that the long-range magnetic order in heterometallic warwickites can appear as a consequence of the cation and charge order. The latter, in turn, arises from the ordering of the J-T distortions. The ability of the system to develop the long-range pattern of the octahedral distortions results in the appearance of the charge ordering. This analysis is useful in understanding the basic electronic and magnetic properties of the warwickites.

Acknowledgements

The reported study was funded by the Russian Foundation for Basic Research (no. 20-02-00559), Government of Krasnoyarsk Territory, Krasnoyarsk Regional Fund of Science to the research project № 18-42-243007.

References

[1] Bloise, A., and E. Barrese. "Synthesis of isomorphic vonsenite-ludwigite series." Neues Jahrbuch für Mineralogie-Abhandlungen: Journal of Mineralogy and Geochemistry 186, (2009): 345–350. https://doi.org/10.1127/0077-7757/2009/0153

[2] Appel, P. W. U., S. Bigi, and M. F. Brigatti. "Crystal structure and chemistry of yuanfuliite and its relationships with warwickite." European Journal of Mineralogy (1999): 483–492. DOI: 10.1127/ejm/11/3/0483

[3] Attfield, J. P., J. F. Clarke, and D. A. Perkins. "Magnetic and crystal structures of iron borates." Physica B: Condensed Matter 180 (1992): 581–584. https://doi.org/10.1016/0921-4526(92)90401-D

[4] Bordet, P., and E. Suard. "Magnetic structure and charge ordering in Fe_3BO_5: A single-crystal x-ray and neutron powder diffraction study." Physical Review B 79 (2009): 144408. https://doi.org/10.1103/PhysRevB.79.144408

[5] Bartolomé, J., A. Arauzo, N. V. Kazak, N. B. Ivanova, S. G. Ovchinnikov, Yu V. Knyazev, and I. S. Lyubutin. "Uniaxial magnetic anisotropy in $Co_{2.25}Fe_{0.75}O_2BO_3$ compared to $Co_3O_2BO_3$ and $Fe_3O_2BO_3$ ludwigites." Physical Review B 83 (2011): 144426. https://doi.org/10.1103/PhysRevB.83.144426

[6] Freitas, D. C., C. P. C. Medrano, D. R. Sanchez, M. N. Regueiro, J. A. Rodríguez-Velamazán, and M. A. Continentino. "Magnetism and charge order in the ladder compound $Co_3O_2BO_3$." Physical Review B 94 (2016): 174409. https://doi.org/10.1103/PhysRevB.94.174409

[7] Larrea, J., D. R. Sanchez, F. J. Litterst, and E. M. Baggio-Saitovitch. "Charge delocalization in the ludwigite $Fe_3O_2BO_3$." Journal of Physics: Condensed Matter 13 (2001): L949. https://doi.org/10.1088/0953-8984/13/48/105

[8] Rappoport, T. G., L. Ghivelder, J. C. Fernandes, R. B. Guimaraes, and M. A. Continentino. "Experimental observation of quantum entanglement in low-dimensional spin systems." Physical Review B 75 (2007): 054422. https://doi.org/10.1103/PhysRevB.75.054422

[9] Guimaraes, R. B., J. C. Fernandes, M. A. Continentino, H. A. Borges, C. S. Moura, J. B. M. Da Cunha, and C. A. Dos Santos. "Dimensional crossover in magnetic warwickites." Physical Review B 56 (1997): 292. https://doi.org/10.1103/PhysRevB.56.292

[10] Hearne, G. R., W. N. Sibanda, E. Carleschi, V. Pischedda, and J. P. Attfield. "Pressure-induced suppression of charge order and nanosecond valence dynamics in Fe_2OBO_3." Physical Review B 86 (2012): 195134. https://doi.org/10.1103/PhysRevB.86.195134

[11] Dong, Maolin, Q. Kuang, X. Zeng, L. Chen, J. Zhu, Q. Fan, Y. Dong, and Y. Zhao. "Mixed-metal borate $FeVBO_4$ of tunnel structure: Synthesis and electrochemical properties in lithium and sodium ion batteries." Journal of Alloys and Compounds 812 (2020): 152165. https://doi.org/10.1016/j.jallcom.2019.152165

[12] Bo, S.-H., C. P. Grey, and P. G. Khalifah. "Defect-Tolerant Diffusion Channels for Mg^{2+} Ions in Ribbon-Type Borates: Structural Insights into Potential Battery Cathodes $MgVBO_4$ and $Mg_xFe_{2-x}B_2O_5$." Chemistry of Materials 27 (2015): 4630–4639. https://doi.org/10.1021/acs.chemmater.5b01040

[13] Pralong, V., B. Le Roux, S. Malo, A. Guesdon, F. Lainé, J. F. Colin, and C. Martin. "Electrochemical activity in oxyborates toward lithium." Journal of Solid State Chemistry 255 (2017): 167-171. https://doi.org/10.1016/j.jssc.2017.08.010

[14] Neuendorf, H., and W. Gunβer. "Transition from quasi-one-dimensional to spin-glass behaviour in insulating $FeMg_2BO_5$." Journal of Magnetism and Magnetic Materials 173 (1997): 117–125. https://doi.org/10.1016/S0304-8853(97)00171-6

[15] Ma, R., D. Xu, Y. Yang, X. Su, B. Lei, Z. Yang, and S. Pan. "$ScMO(BO_3)$ (M = Ca and Cd): new Sc-based oxyborates featuring interesting edge-sharing sandwich-like chains and UV cut-off edges." Dalton Transactions 46 (2017): 14839–14846. 10.1039/C7DT03172F

[16] Kumar, J., S. N. Panja, D. J. Mukkattukavil, A. Bhattacharyya, A. K. Nigam, and S. Nair. "Reentrant superspin glass state and magnetization steps in the oxyborate Co_2AlBO_5." Physical Review B 95 (2017): 144409. https://doi.org/10.1103/PhysRevB.95.144409

[17] Arauzo, A., N. V. Kazak, N. B. Ivanova, M. S. Platunov, Y. V. Knyazev, O. A. Bayukov, L. N. Bezmaternykh, I. S. Lyubutin, K. V. Frolov, S. G. Ovchinnikov, and J. Bartolomé. "Spin-glass behavior in single crystals of hetero-metallic magnetic warwickites $MgFeBO_4$, $Mg_{0.5}Co_{0.5}FeBO_4$, and $CoFeBO_4$." Journal of Magnetism and Magnetic Materials 392 (2015) 114–125. https://doi.org/10.1016/j.jmmm.2015.05.006

[18] Lyubutin, I. S., N. Yu Korotkov, K. V. Frolov, N. V. Kazak, M. S. Platunov, Yu V. Knyazev, L. N. Bezmaternykh, S. G. Ovchinnikov, A. Arauzo, and J. Bartolomé. "Spin-glass behavior of warwickite $MgFeBO_4$ and $CoFeBO_4$ crystals observed by Mössbauer spectroscopy." Journal of Alloys and Compounds 642 (2015): 204-209. https://doi.org/10.1016/j.jallcom.2015.04.067

[19] Fernandes, J. C., R. B. Guimaraes, M. A. Continentino, H. A. Borges, J. V. Valarelli, and A. Lacerda. "Titanium-III warwickites: A family of one-dimensional disordered magnetic systems." Physical Review B 50 (1994): 16754. https://doi.org/10.1103/PhysRevB.50.16754

[20] Goff, R. J., A. J. Williams, and J. P. Attfield. "Spin, charge, and orbital order in Mn_2OBO_3." Physical Review B 70 (2004): 014426. https://doi.org/10.1103/PhysRevB.70.014426

[21] Kazak, N. V., M. S. Platunov, Yu V. Knyazev, N. B. Ivanova, O. A. Bayukov, A. D. Vasiliev, L. N. Bezmaternykh et al. "Uniaxial anisotropy and low-temperature antiferromagnetism of Mn_2BO_4 single crystal." Journal of Magnetism and Magnetic Materials 393 (2015): 316–324. https://doi.org/10.1016/j.jmmm.2015.05.081

[22] Attfield, J. P., A. M. T. Bell, L. M. Rodriguez-Martinez, J. M. Greneche, R. J. Cernik, J. F. Clarke, and D. A. Perkins. "Electrostatically driven charge-ordering in Fe_2OBO_3." Nature 396 (1998): 655. https://doi.org/10.1038/25309

[23] Carnicom, E. M., K. Górnicka, T. Klimczuk, and R. J. Cava. "The homometallic warwickite V_2OBO_3." Journal of Solid State Chemistry 265 (2018): 319–325. https://doi.org/10.1016/j.jssc.2018.06.021

[24] Kazak, N. V., M. S. Platunov, Yu V. Knyazev, E. M. Moshkina, S. Yu Gavrilkin, O. A. Bayukov, M. V. Gorev et al. "Fe-induced enhancement of antiferromagnetic spin correlations in $Mn_{2-x}Fe_xBO_4$." Journal of Magnetism and Magnetic Materials 452 (2018): 90–99. https://doi.org/10.1016/j.jmmm.2017.12.037

[25] M.S. Platunov, N.V. Kazak, Yu.V. Knyazev, L.N. Bezmaternykh, E.M. Moshkina, A.L. Trigub, A.A. Veligzhanin, Y.V. Zubavichus, L.A. Solovyov, D.A. Velikanov, S.G. Ovchinnikov, Effect of Fe-substitution on the structure and magnetism of single crystals $Mn_{2-x}Fe_xBO_4$, Journal of Crystal Growth 475 (2017): 239–246. https://doi.org/10.1016/j.jcrysgro.2017.06.026

[26] R. D. Shannon, Acta Crystallogr. A 32 (1976): 751. https://doi.org/10.1107/S0567739476001551

[27] Norrestam, R. "Structural investigation of two synthetic warwickites: Undistorted orthorhombic $MgScOBO_3$ and distorted monoclinic $Mg_{0.76}Mn_{1.24}OBO_3$." Zeitschrift für Kristallographie-Crystalline Materials 189 (1989): 1–12. https://doi.org/10.1524/zkri.1989.189.14.1

[28] Eremina, R. M., E. M. Moshkina, A. R. Muftakhutdinov, I. F. Gilmutdinov, and N. M. Lyadov. "Magnetic properties of the warwickite $MnMgBO_4$." Solid State Communications 290 (2019): 64–66. https://doi.org/10.1016/j.ssc.2018.12.019

[29] G.M. Sheldrick. A short history of SHELX. Acta Cryst. A, 64 (2008) 112–122. https://doi.org/10.1107/S0108767307043930

[30] Sheldrick, G. M. SHELXS and SHELXL97. *Program for Crystal Structure Refinement*, University of Göttingen, Germany (1997).

[31] I.D. Brown, D. Altermatt, Acta Cryst. B 41 (1985) 244–247. https://doi.org/10.1107/S0108768185002063

[32] Tetsuya Kawano and Hisanori Yamane. "Redetermination of synthetic warwickite, $Mg_3TiO_2(BO_3)_2$." Acta Crystallographica Section E 67 (2011): i18–i19. https://doi.org/10.1107/S1600536811002157

[33] N.V. Kazak, M.S. Platunov, Yu.V. Knyazev, N.B. Ivanova, Y.V. Zubavichus, A.A. Veligzhanin, A.D. Vasiliev, L.N. Bezmaternykh, O.A. Bayukov, A. Arauzo, J. Bartolome, K.V. Lamonova, and S.G. Ovchinnikov. "Crystal and local atomic structure of $MgFeBO_4$, $Mg_{0.5}Co_{0.5}FeBO_4$, and $CoFeBO_4$: Effects of Co substitution." Phys. Status Solidi B 252 (2015): 2245–2258. https://doi.org/10.1002/pssb.201552143

[34] Yang, Z., X. L. Chen, J. K. Liang, Y. C. Lan, and T. Xu. "Phase relations in the MgO–Ga_2O_3–B_2O_3 system and the crystal structure of $MgGaBO_4$." Journal of Alloys and Compounds 319 (2001): 247–252. https://doi.org/10.1016/S0925-8388(01)00871-4

[35] Li, H. K., G. M. Cai, J. J. Fan, Z. P. Jin, T. T. Zhou, and X. L. Chen. "Crystal structures of two novel borate compounds $MgInBO_4$ and MgIn7/8B7/8O29/8." Journal of Solid State Chemistry 202 (2013): 262–268. https://doi.org/10.1016/j.jssc.2013.03.060

[36] Kawano, T., and H. Yamane. "Synthesis, crystal structures and photoluminescence properties of new oxyborates, $Mg_5NbO_3(BO_3)_3$ and $Mg_5TaO_3(BO_3)_3$, with novel warwickite-type superstructures." Journal of Solid State Chemistry 184 (2011): 2466–2471. https://doi.org/10.1016/j.jssc.2011.07.022

[37] Needle-shaped single crystals of $Co_5NbB_3O_{12}$ were grown using the flux method. The crystal structure characterisation was completed using the SMART APEX II single crystal diffractometer; orthorhombic space group Pbnm(62) with a = 9.3336(7), b = 9.4039(7) Å, c = 3.1793(2) Å, V = 279.05(3), Z = 8. The structure was solved by direct methods using the SHELXS program. The structure refinement was carried out by least-square minimization in SHELXL program using anisotropic thermal parameters of all atoms. The final indexes are R1 = 0.0309, wR2 = 0.0715, Goodness-of-fit on F2 = 1.051. The *dc* magnetisation and heat capacity experiments were performed. The results are prepared for the publication.

[38] M. Angst, P. Khalifah, R.P. Hermann, H.J. Xiang, M.-H. Whangbo, V. Varadarajan, J.W. Brill, B.C. Sales, and D. Mandrus. "Charge Order Superstructure with Integer Iron Valence in Fe_2OBO_3." Physical review letters 99 (2007): 086403. https://doi.org/10.1103/PhysRevLett.99.086403

Appendix

Table A1. Crystallographic data and main parameters of processing and refinement of $Mn_{2-x}Mg_xBO_4$.

	$Mn_{1.45}Mg_{0.55}BO_4$	$Mn_{1.37}Mg_{0.63}BO_4$	$Mn_{1.33}Mg_{0.67}BO_4$
		Crystal data	
M_r		154.06	
Symmetry		monoclinic	
Space group		P 1 21/n 1	
Z		2	
T, K		296	
a, Å	9.2920(3)	9.2939(4)	9.2887(13)
b, Å	9.3966(3)	9.3725(4)	9.3467(13)
c, Å	3.2052(1)	3.1972(1)	3.1876(5)
β, °	90.619(1)	90.539(1)	90.312(3)
V, Å^3	279.84(2)	278.49(2)	276.74(7)
D_x, g/cm^{-3}	1.828	1.837	1.849
μ, mm^{-1}	2.374	2.385	2.401
		Data collection	
Wavelength		MoKα, λ= 0.71073Å	
F (000)		148	
θ, °	3.08-37.99	3.08-36.97	3.09-36.98
H	-15 → 16	-15 → 15	-15 → 15
K	-16 → 16	-15 → 15	-15 → 15
L	-5 → 5	-5 → 5	-5 → 5
Measured reflections	6139	5820	5455
Independent reflections	1516	1415	1397
Reflections with I>2σ(I)	1280	1298	1296
Extinction	0.031(2)	0.033(3)	0.074(14)
goodness-of-fit on F^2	1.045	1.141	3.409
final R indices			
R1	0.0280	0.0252	0.1011
wR2	0.0559	0.0575	0.2251

Table A2. Atomic coordinates and isotropic thermal parameters (Å^2).

	S.O.F.	*x*	*y*	*z*	U_{iso}
			$Mn_{1.45}Mg_{0.55}BO_4$		
Mn1	0.936	0.55926(3)	0.38244(3)	0.28265(8)	0.00620(8)
Mg1	0.064	0.55926(3)	0.38244(3)	0.28265(8)	0.00620(8)
Mn2	0.517	0.82501(4)	0.59943(4)	0.71756(11)	0.00843(11)
Mg2	0.483	0.82501(4)	0.59943(4)	0.71756(11)	0.00843(11)
O3		0.38758(13)	0.48862(13)	0.2845(4)	0.0084(2)
O4		0.99224(13)	0.25683(14)	0.3579(4)	0.0098(2)
O5		0.86866(14)	0.47154(14)	0.2202(4)	0.0119(3)
O6		0.73291(14)	0.26029(13)	0.3210(4)	0.0107(3)
B7		0.86431(19)	0.3312(2)	0.3002(6)	0.0081(3)
			$Mn_{1.37}Mg_{0.63}BO_4$		
Mn1	0.940	0.55965(3)	0.38214(3)	0.28175(8)	0.00552(8)
Mg1	0.060	0.55965(3)	0.38214(3)	0.28175(8)	0.00552(8)
Mn2	0.433	0.82382(4)	0.59995(4)	0.71722(12)	0.00781(12)
Mg2	0.567	0.82382(4)	0.59995(4)	0.71722(12)	0.00781(12)
O1		0.38755(12)	0.48802(13)	0.2836(4)	0.0079(2)
O2		0.73378(13)	0.25988(13)	0.3197(4)	0.0097(2)
O3		0.99317(13)	0.25778(13)	0.3550(4)	0.0094(2)
O4		0.86782(14)	0.47292(13)	0.2206(4)	0.0113(2)
B		0.86427(18)	0.33248(19)	0.2989(6)	0.0075(3)

$Mn_{1.33}Mg_{0.67}BO_4$					
Mn1	0.960	0.56007(10)	0.38197(10)	0.2776(3)	0.0070(3)
Mg1	0.040	0.56007(10)	0.38197(10)	0.2776(3)	0.0070(3)
Mn2	0.368	0.82275(18)	0.60045(16)	0.7213(5)	0.0095(5)
Mg2	0.632	0.82275(18)	0.60045(16)	0.7213(5)	0.0095(5)
O1		0.3876(5)	0.4878(5)	0.2774(16)	0.0091(9)
O2		0.7347(5)	0.2598(5)	0.3148(18)	0.0126(10)
O3		0.9937(5)	0.2581(5)	0.3491(17)	0.0131(10)
O4		0.8675(5)	0.4740(5)	0.2250(17)	0.0126(10)
B		0.8645(7)	0.3338(8)	0.296(2)	0.0088(11)

Table A3. Anisotropic displacement parameters ($Å^2$).

Atom	U_{11}	U_{22}	U_{33}	U_{12}	U_{13}	U_{23}
$Mn_{1.45}Mg_{0.55}BO_4$						
Mn1|Mg1	0.00509(12)	0.00635(12)	0.00715(12)	0.00077(8)	-0.00105(8)	-0.00089(8)
Mn2|Mg2	0.00916(18)	0.00760(17)	0.00854(17)	-0.00165(11)	0.00031(11)	-0.00046(11)
O003	0.0074(5)	0.0090(5)	0.0089(5)	0.0004(4)	-0.0004(4)	-0.0004(4)
O004	0.0071(5)	0.0101(5)	0.0123(5)	0.0019(4)	-0.0010(4)	0.0011(4)
O005	0.0117(6)	0.0085(5)	0.0155(6)	-0.0003(4)	0.0005(5)	0.0012(4)
O006	0.0068(5)	0.0095(5)	0.0158(6)	0.0004(4)	-0.0004(4)	0.0001(4)
B007	0.0064(7)	0.0107(8)	0.0072(7)	0.0005(5)	-0.0005(5)	-0.0002(6)
$Mn_{1.37}Mg_{0.63}BO_4$						
Mn1|Mg1	0.00369(11)	0.00537(11)	0.00748(11)	0.00089(7)	-0.00077(7)	-0.00080(7)
Mn2|Mg2	0.00806(18)	0.00651(17)	0.00887(17)	-0.00169(11)	0.00033(11)	-0.00027(11)
O1	0.0050(4)	0.0088(5)	0.0100(5)	0.0009(4)	-0.0003(4)	-0.0001(4)
O2	0.0048(4)	0.0087(5)	0.0155(5)	-0.0003(4)	0.0000(4)	0.0007(4)
O3	0.0056(4)	0.0102(5)	0.0123(5)	0.0014(4)	0.0000(4)	0.0010(4)
O4	0.0107(5)	0.0079(5)	0.0153(6)	-0.0001(4)	0.0002(4)	0.0015(4)
B	0.0045(6)	0.0084(7)	0.0095(7)	0.0005(5)	-0.0001(5)	0.0005(5)
$Mn_{1.33}Mg_{0.67}BO_4$						
Mn1|Mg1	0.0050(4)	0.0052(4)	0.0108(5)	0.0008(3)	-0.0010(3)	-0.0008(3)
Mn2|Mg2	0.0098(8)	0.0063(7)	0.0124(8)	-0.0019(4)	0.0000(5)	-0.0002(5)
O1	0.0053(17)	0.0079(18)	0.014(2)	0.0005(13)	0.0008(15)	0.0003(15)
O2	0.0064(18)	0.010(2)	0.021(2)	0.0000(14)	-0.0012(17)	-0.0003(17)
O3	0.0089(19)	0.012(2)	0.018(2)	0.0007(15)	0.0007(17)	0.0006(17)
O4	0.013(2)	0.0068(18)	0.018(2)	-0.0006(14)	0.0004(18)	0.0013(16)
B	0.005(2)	0.009(3)	0.012(3)	-0.0002(19)	0.001(2)	0.002(2)

Table A4. Selected bond lengths (Å) for $Mn_{2-x}Mg_xBO_4$.

Mn_2BO_4		$Mn1_{.45}Mg_{0.55}BO_4$		$Mn_{1.37}Mg_{0.63}BO_4$		$Mn_{1.33}Mg_{0.67}BO_4$	
Mn1—O3	1.8842(10)	Mn1|Mg1—O003	1.8816(13)	Mn1|Mg1—O1	1.8824(12)	Mn1|Mg1—O1	1.883(5)
Mn1—O3^{i}	1.9043(10)	Mn1|Mg1—O003^{i}	1.9032(12)	Mn1|Mg1—O1^{i}	1.9078(12)	Mn1|Mg1—O1^{i}	1.930(5)
Mn1—O1	1.9745(10)	Mn1|Mg1—O004^{ii}	1.9839(13)	Mn1|Mg1—O3^{ii}	1.9868(12)	Mn1|Mg1—O3^{ii}	1.988(5)
Mn1—O4	1.978(1)	Mn1|Mg1—O006	1.9829(13)	Mn1|Mg1—O2	1.9857(12)	Mn1|Mg1—O2	1.987(5)
Mn1—O3^{ii}	2.2699(10)	Mn1|Mg1—O003^{iii}	2.2440(12)	Mn1|Mg1—O1^{iii}	2.2374(12)	Mn1|Mg1—O1^{iii}	2.204(5)
Mn1—O1^{iii}	2.379(1)	Mn1|Mg1—O004^{iv}	2.3504(13)	Mn1|Mg1—O3^{iv}	2.3413(13)	Mn1|Mg1—O3^{iv}	2.329(5)
Mn2—O2	2.0881(10)	Mn2|Mg2—O005	2.0405(14)	Mg2|Mn2—O4	2.0292(14)	Mg2|Mn2—O4	2.020(5)
Mn2—O2^{iv}	2.0939(10)	Mn2|Mg2—O005^{vi}	2.0470(14)	Mg2|Mn2—O4^{v}	2.0402(13)	Mg2|Mn2—O4^{v}	2.035(5)
Mn2—O3^{v}	2.1858(10)	Mn2|Mg2—O003^{i}	2.1416(13)	Mg2|Mn2—O1^{i}	2.1305(12)	Mg2|Mn2—O1^{i}	2.120(5)
Mn2—O4^{iv}	2.2222(10)	Mn2|Mg2—O006^{viii}	2.1861(13)	Mg2|Mn2—O2^{vii}	2.1773(13)	Mg2|Mn2—O2^{vi}	2.168(6)
Mn2—O1	2.2479(10)	Mn2|Mg2—O004^{vii}	2.1853(13)	Mg2|Mn2—O3^{vi}	2.1752(13)	Mg2|Mn2—O3^{vii}	2.171(5)

Mn2—O4	2.4236(11)	Mn2|Mg2—O006^{ix}	2.3525(14)	Mg2|Mn2—O2^{viii}	2.3374(13)	Mg2|Mn2—O2^{viii}	2.327(6)
B—O2^{vi}	1.3477(19)	B007—O005	1.344(2)	B—O4	1.340(2)	B—O4	1.330(9)
B—O4^{ix}	1.3882(18)	B007—O006	1.393(2)	B—O2	1.393(2)	B—O2	1.392(8)
B—O1	1.3924(17)	B007—O004	1.390(2)	B—O3	1.398(2)	B—O3	1.403(8)
<B-O>	1.376		1.376		1.377		1.375